Beam Tests of AHCAL Prototype

Hongbin Diao

May 9, 2026

Abstract

The Circular Electron Positron Collider (CEPC) is a proposed next-generation collider designed for precision measurements of Higgs boson properties. A primary challenge for the CEPC detector is achieving a boson mass resolution (BMR) of 4%, which is essential for distinguishing Higgs, Z, and W bosons in their hadronic decay modes. The baseline detector design adopts the Particle Flow Algorithm (PFA) concept to satisfy this requirement, where BMR performance is largely governed by the shower separation capability and energy resolution of the calorimetry system. Consequently, a high-granularity hadronic calorimeter is indispensable.In this study, we evaluate an Analogue Hadron Calorimeter (AHCAL) prototype—a scintillator-based option with analogue readout—which underwent beam tests at CERN. Fundamental parameters of the prototype were calibrated, and a comprehensive Geant4-based simulation was developed to establish a robust digitization model. By validating the simulation against reconstructed beam test data, we demonstrated that the energy linearity for pions is maintained within $\pm 1.5\%$, achieving an energy resolution of $48.8\%/\sqrt{E[\mathrm{GeV}]} \oplus 4.5\%$.

1 Introduction

The discovery of the Higgs boson marked a major milestone in particle physics [1, 2]. The subsequent priority is the precise determination of its properties [3, 4, 5, 6]. The Circular Electron–Positron Collider (CEPC), proposed by the Chinese high energy physics community, is designed as a Higgs factory dedicated to precision measurements of the Higgs boson[7, 8]. The CEPC is planned to operate at a center-of-mass energy of 240 GeV with a design luminosity of 8.3×10^{34} cm^{-2}s^{-1}, yielding approximately 10^6 Higgs bosons over a decade of operation[9].

A large fraction of Higgs production events at the CEPC result in final states containing hadronic jets originating from the decays of the Higgs, Z, and W bosons. Precise jet energy reconstruction is therefore essential, with a target boson mass resolution (BMR) of about 4% in hadronic decay channels, enabling the separation of Higgs, Z, and W bosons. To meet this requirement, the baseline CEPC detector design is guided by the particle flow algorithm (PFA), in which individual particles in a jet are reconstructed separately, and their energies are measured using the most suitable subdetector[10, 11]. The jet energy is then obtained by combining these measurements, aiming at a jet energy resolution of 3–4% for jets in the energy range of 50–100 GeV[12].

A critical requirement for the successful implementation of PFA at the CEPC is the efficient separation of nearby particles within jets in the calorimeter system. This necessitates a calorimeter with high spatial granularity. Several technological options have been proposed for the hadronic calorimeter (HCAL) of the CEPC detector to fulfill these requirements. One such option is a scintillator–steel HCAL with analogue readout (AHCAL)[13, 14, 15]. The high gran-

ularity of the CEPC AHCAL provides the shower separation capability essential for PFA-based jet reconstruction. Considering these, a AHCAL prototype has been constructed.

Based on the optimized AHCAL design, the prototype is expected to achieve an energy linearity of about 1.5% and an energy resolution of approximately $60\%/\sqrt{E\ (\mathrm{GeV})}$ for pion beams in the energy range of 10–80 GeV[16].

The prototype consists of 40 sampling layers, each comprising a 20 mm thick steel absorber and plastic scintillator tiles with dimensions of $40\times40\times3\ \mathrm{mm}^3$ as the active material, as illustrated in Fig. 1. The total depth of the prototype corresponds to approximately $5\,\lambda$, ensuring adequate containment of hadronic showers.

The sensitive area of the prototype is $720 \times 720\ \mathrm{mm}^2$, corresponding to a total of 12,960 scintillator tiles. The scintillation signals are read out by silicon photomultipliers (SiPMs) and processed using SPIROC2E[17, 18].

The scintillator tiles and front-end electronics are integrated into steel cassettes to form individual sensitive layers, which are assembled together with the absorber plates within a mechanical support structure[19].

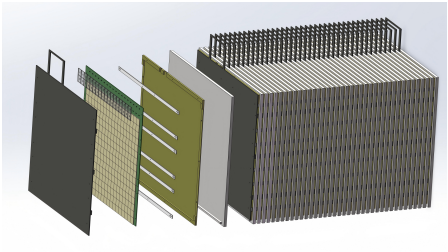

Figure 1: The scintillator-steel sandwich structure of the AHCAL prototype. The scintillator tiles and PCB board were housed within the steel cassette, creating a sensitive layer for the AHCAL.

2 Beam Test Setup

The AHCAL prototype has been tested three times at CERN using high energy particle beams, including H8 and H2 beamline at SPS and T9 beamline at PS. Each time of beam test last two weeks. During these periods, we completed detector commissioning and electronics calibration, and collected a large dataset of particles including $\mu^{\pm}$, $e^{\pm}$ and $\pi^{\pm}$ with the momentum of $1GeV$ to $120GeV$

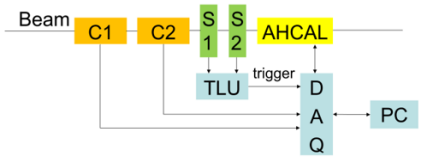

Figure 2: Beam test layout of AHCAL prototype

As Fig. 2 shows, The beam first passes through two Cherenkov detectors used for particle identification, followed by two scintillator detectors for coincidence measurements, and finally

enters the AHCAL prototype. The signals from the two Cherenkov detectors (C1 and C2) are sent to the DAQ board, while the signals from the two scintillator detectors (S1 and S2) are sent to the TLU for coincidence processing. Based on the coincidence result, the TLU determines whether to issue a trigger to the DAQ board. Upon receiving the trigger, the DAQ board collects AHCAL data and packages it together with the Cherenkov detector data for transmission to the PC.

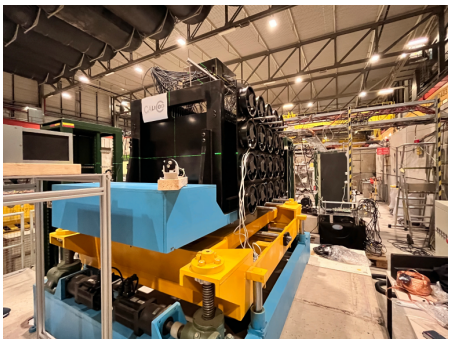

Figure 3: AHCAL prototype at H8 beamline of SPS

3 Calibration of Basic Parameters

To fully characterize the detector response and ensure data integrity across a wide dynamic range, a systematic calibration procedure was implemented. This process encompasses the determination of the electronic pedestal, the the high-to-low gain (HG/LG) ratios, the energy scale via Minimum Ionizing Particles (MIPs), and single photoelectron (SPE) gain.

The pedestals of both the high and low-gain channels were obtained through an external trigger. Figure 4 depicts the distributions of pedestals for all AHCAL high gain channels and low gain channels.

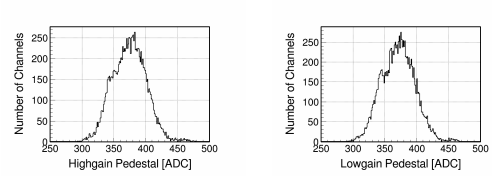

(a) (b)

Figure 4: Pedestal of AHCAL prototype: (a) highgain channels. (b) lowgain channels

The gain ratios and saturation points of all AHCAL channels were calibrated using pion beam. The distributions of the gain ratios and saturation points are shown in Fig. 5.

The Minimum Ionizing Particle (MIP) response for each channel was calibrated using a muon beam. During the beam test, the prototype was mounted on a translation stage, which was used to adjust its position and facilitate a comprehensive muon scan across all target areas. Consequently, sufficient statistics were obtained for MIP calibration in nearly all channels, with

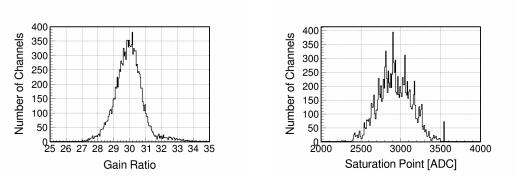

(a) (b)

Figure 5: Gain ratio calibration of AHCAL prototype: (a) gain ratio. (b) highgain saturation point

the exception of those at the periphery. The Most Probable Value (MPV) was extracted from the MIP spectra by performing a fit with a Landau-convolved Gaussian function.

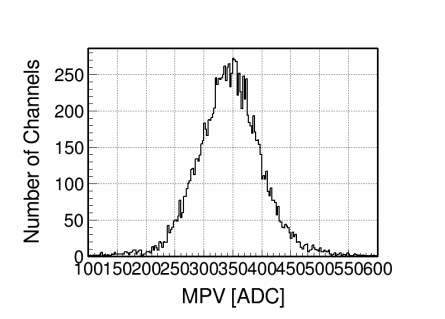

Figure 6: MPV of AHCAL prototype

The single photoelectron (SPE) response for each channel was also calibrated using a muon beam. A multi-Gaussian function was employed to fit the SPE spectrum, allowing for the precise determination of the individual photoelectron peak positions.

Fig. 8 showes that the distribution of these basic parameters calibrated in layer level. Within the same layer—or more specifically, within the same chip-the parameter variation across different channels is relatively small, whereas the variation between layers or across different chips is more significant. For gain ratio and spe, the last two layers seems different with others, this is because they use different model of SiPM, making the waveform is differnet.

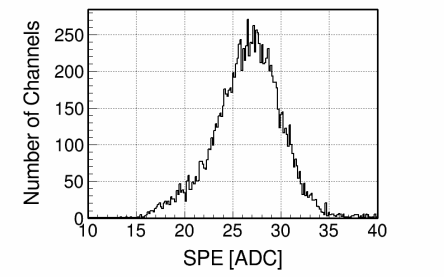

Figure 7: SPE of AHCAL prototype

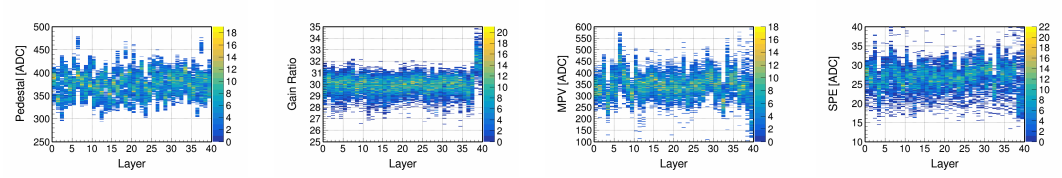

(a) (b) (c) (d)

Figure 8: Layer distribution of basic parameters calibrated: (a) Highgain pedestal. (b) Gain Ratio. (c) MPV. (d) SPE

4 Results

After calibration above, we can reconstruct energy using formula 1

$$E_i^{\mathrm{Dep}}\,[\mathrm{MeV}] = \begin{cases} \dfrac{HS_i - HP_i}{C_i^{\mathrm{ADC}\to\mathrm{MIP}} \times C^{\mathrm{MIP}\to\mathrm{MeV}}}, & HS_i < SP_i \\ \dfrac{(LS_i - LP_i) \times C_i^{\mathrm{LG}\to\mathrm{HG}}}{C_i^{\mathrm{ADC}\to\mathrm{MIP}} \times C^{\mathrm{MIP}\to\mathrm{MeV}}}, & HS_i > SP_i \end{cases} \tag{1}$$

The deposited energy in the i-th sensitive cell, E_i^{Dep}, is reconstructed from the high and low-gain channel signals HS_i and LS_i, together with calibration parameters HP_i, LP_i, SP_i, $C_i^{\mathrm{LG}\to\mathrm{HG}}$, $C_i^{\mathrm{ADC}\to\mathrm{MIP}}$, and $C^{\mathrm{MIP}\to\mathrm{MeV}}$.

Here, HP_i and LP_i are the pedestals of the high and low-gain channels, respectively, and SP_i is the saturation point of the high-gain channel. When $HS_i < SP_i$, the deposited energy is reconstructed using the high-gain signal HS_i. When $HS_i > SP_i$, the low-gain signal LS_i is used, multiplied by the high-to-low gain conversion factor $C_i^{\mathrm{LG}\to\mathrm{HG}}$.

The conversion factor $C_i^{\mathrm{ADC}\to\mathrm{MIP}}$ is obtained from muon beam calibration data. The energy deposition spectrum of muons in each sensitive cell is fitted with a Landau distribution convoluted with a Gaussian function. The most probable value (MPV) of the Landau distribution is taken as $C_i^{\mathrm{ADC}\to\mathrm{MIP}}$.

The conversion factor $C^{\mathrm{MIP}\to\mathrm{MeV}}$ is determined from GEANT4 simulation of the AHCAL response to 100 GeV muons. The energy deposition spectrum of 100 GeV muons in a sensitive cell is fitted with a Landau function, yielding an MPV of 0.461 MeV. Therefore,

$$C^{\mathrm{MIP}\to\mathrm{MeV}} = \frac{\mathrm{MIP}}{0.461\ \mathrm{MeV}}. \tag{2}$$

Due to the presence of beam contaminants, a series of event selection criteria and Particle Identification (PID) techniques were applied to the raw beam data. Using these PID methods, we effectively suppressed the background[20]. This ensured that the energy spectra were reconstructed from a highly pure sample.

In addition, a high-fidelity Geant4-based simulation was conducted. To bridge the gap between simulated energy deposition and experimental observables, we developed a comprehensive digitization model. This model converts the simulation raw data into realistic detector responses by incorporating the fundamental calorimeter parameters calibrated previously. The digitization chain accounts for several critical physical effects: the statistical fluctuations of scintillation photons, the spatial non-uniformity of light yield within the scintillator, the SiPM photon detection efficiency, and the signal shaping and electronic noise of the readout system. The simulation results can be compared with the beam test data to validate the accuracy of the digitization model and the energy reconstruction algorithm.

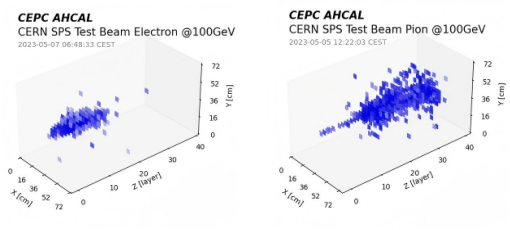

(a) (b)

Figure 9: Beam test event displays of the AHCAL prototype: (a) a 100 GeV e^- beam event. (b) a 100 GeV π^- beam event.

4.1 Electron Beam

At the PS, the electron beam energy ranges from 1 GeV to 5 GeV. Hear the energy linearity could be within ±2%, if ignore energy point of 1 GeV, it can be within ±1.5%. At the SPS, the electron beam energy ranges from 10 GeV to 250 GeV. At these levels, the energy deposition in a single cell is sufficiently high to cause significant saturation in both the SiPM and the electronics. As shown in Fig. 11(b), the peak position of the beam data and the digitized MC is notably lower than that of the MC without digitization. And as shown in 15(b), the visible deposit energy of beam data and MC with digitization gradually bends downward and is significantly lower than the MC without digitization. Furthermore, variations between different channels introduce additional fluctuations that scale with the beam energy. This causes the energy resolution become worse at high energy. And the saturation do not affect the number of hit, which is only related to the shape of shower, so the agreement of this between beam data and MC without digitization is good.

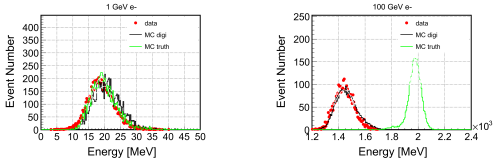

(a) (b)

Figure 10: Total energy deposition of electron beam, red point is the beam data, green line is the MC without digitization, black line is the MC with digitization: (a) 1 GeV at PS. (b) 100 GeV at SPS

4.2 Pion Beam

At the PS, the pion beam energy ranges from 1 GeV to 15 GeV. At the SPS, the pion beam energy ranges from 20 GeV to 100 GeV. Hadronic showers are less collimated and more widely distributed than electromagnetic showers; consequently, the energy deposition within a single cell is relatively low, making saturation effects significantly less pronounced, especially for electronics. But it still exist SiPM saturation effect, resulting in peak of deposit energy of beam data and MC with digitization lower than MC without digitization. And this effect is same for all channels,

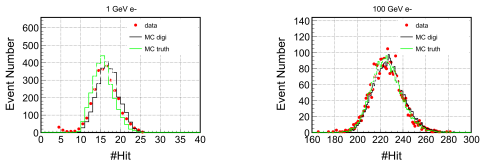

(a) (b)

Figure 11: Total number of hit of electron beam: (a) 1 GeV at PS. (b) 100 GeV at SPS

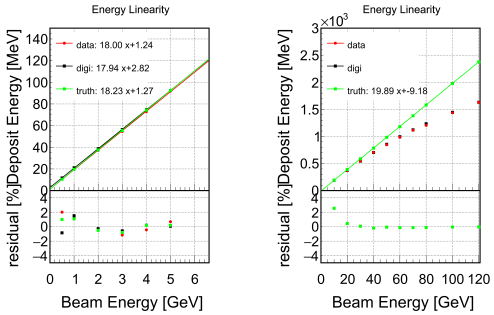

(a) (b)

Figure 12: Energy linearity of electron: (a) energy range of 1 GeV-5 GeV at PS. (b) energy range of 10 GeV-150 GeV at SPS

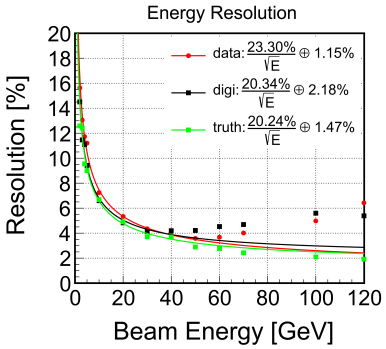

Figure 13: Resolution of electron beam with energy range of 1 GeV-100 GeV

so it will not introduce additional flutuation like electronics. Conversely, the saturation effect suppresses the high-energy region, effectively narrowing the energy spectrum and making the energy resolution appear smaller. Ultimately, the energy linearity for pions beam data was maintained within ±1.5%, and an energy resolution of $48.8\%/\sqrt{E[\mathrm{GeV}]} \oplus 4.5\%$ was achieved.

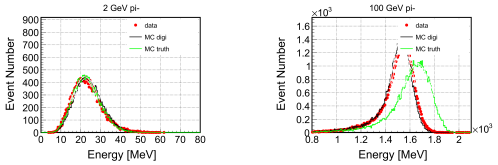

(a) (b)

Figure 14: Total energy deposition of pion beam: (a) 2 GeV at PS. (b) 100 GeV at SPS

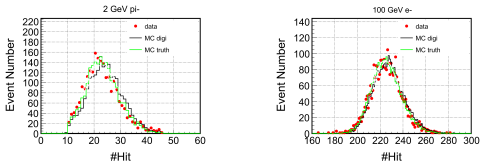

(a) (b)

Figure 15: Total number of hit of pion beam: (a) 2 GeV at PS. (b) 100 GeV at SPS

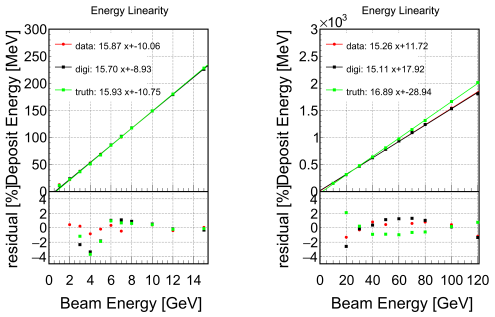

(a) (b)

Figure 16: Energy linearity of pion: (a) energy range of 1 GeV-5 GeV at PS. (b) energy range of 10 GeV-150 GeV at SPS

5 Summary

A series of three beam tests were successfully conducted for the AHCAL prototype at CERN. Environmental and operational stability was ensured by monitoring temperature, pedestals, gain ratios, and MIP responses. These efforts yielded a comprehensive dataset comprising electronics test results and roughly 68 million particle events (μ, π, e). Calibration of channel-specific parameters—including pedestals, gain ratios, saturation points, Most Probable Values (MPV) and Single PhotonElectron (SPE)—was performed to reconstruct the energy deposition across all sensitive cells. Effective particle identification (PID) based on energy and topological information enabled the selection of a high-purity π^- sample. For e^-, because of the saturation effect of SiPM and electronics, the energy linearity become bad beyond 30 GeV, and the energy

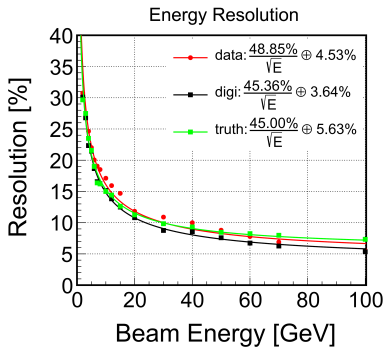

Figure 17: Resolution of pion beam with energy range of 1 GeV-100 GeV

resolution increase alone with the beam energy.For π^- energies in the range of 10–100 GeV, the saturation effective is not obvirous, so the prototype achieved a high energy linearity of $\pm 1.5\%$ and a energy resolution of $48.8\%/\sqrt{E[\mathrm{GeV}]} \oplus 4.5\%$. In future, a refined electrical calibration could be carried out for each individual cell. A known amount of charge will be injected into each cell and the corresponding signal response will be measured. In this way, the saturation curve of each cell can be obtained, enabling subsequent corrections.

References

[1] Cms Collaboration et al. Observation of a new boson at a mass of 125 gev with the cms experiment at the lhc. *arXiv preprint arXiv:1207.7235*, 2012.

[2] Atlas Collaboration et al. Observation of a new particle in the search for the standard model higgs boson with the atlas detector at the lhc. *arXiv preprint arXiv:1207.7214*, 2012.

[3] Zhen-Xing Chen, Ying Yang, Man-Qi Ruan, Da-Yong Wang, Gang Li, Shan Jin, and Yong Ban. Cross section and higgs mass measurement with higgsstrahlung at the cepc. *Chinese Physics C*, 41(2):023003, 2017.

[4] Fenfen An, Yu Bai, Chunhui Chen, Xin Chen, Zhenxing Chen, Joao Guimaraes Da Costa, Zhenwei Cui, Yaquan Fang, Chengdong Fu, Jun Gao, et al. Precision higgs physics at the cepc. *Chinese Physics C*, 43(4):043002, 2019.

[5] Tao Han, Zhen Liu, and Josh Sayre. Potential precision on higgs couplings and total width at the ilc. *Physical Review D*, 89(11):113006, 2014.

[6] Qiyu Sha, Abdualazem Fadol, Fangyi Guo, Gang Li, Yaquan Fang, Jiayin Gu, and Xinchou Lou. Probing higgs cp properties at the cepc in the e+ e-→ zh→ l+ l-h using optimal variables. *The European Physical Journal C*, 82(11):981, 2022.

[7] CEPC Study Group et al. Cepc conceptual design report: Volume 2-physics & detector. *arXiv preprint arXiv:1811.10545*, 2018.

[8] CEPC Study Group et al. Cepc technical design report–reference detector. *arXiv preprint arXiv:2510.05260*, 2025.

[9] Waleed Abdallah, Konstantin Afanaciev, Shakeel Ahmad, Ijaz Ahmed, Xiaocong Ai, Abid Aleem, Wolfgang Altmannshofer, Fabio Alves, Rui An, Weiming An, et al. Cepc technical design report–accelerator. *Radiat. Detect. Technol. Methods*, 8(1):1–1105, 2024.

[10] MA Thomson. Particle flow calorimetry and the pandorapfa algorithm. *Nuclear Instruments and Methods in Physics Research Section A: Accelerators, Spectrometers, Detectors and Associated Equipment*, 611(1):25–40, 2009.

[11] Meng-Yao Liu, Wei-Dong Li, Xing-Tao Huang, Yao Zhang, Tao Lin, and Ye Yuan. Simulation and reconstruction of particle trajectories in the cepc drift chamber. *Nucl. Sci. Tech.*, 35(8):128, 2024.

[12] Yuhang Tan, Xin Shi, Ryuta Kiuchi, Manqi Ruan, Maoqiang Jing, Dan Yu, Kaili Zhang, Xinchou Lou, Xin Mo, Gang Li, et al. Search for invisible decays of the higgs boson produced at the cepc. *Chinese Physics C*, 44(12):123001, 2020.

[13] Felix Sefkow, Frank Simon, and CALICE collaboration. A highly granular sipm-on-tile calorimeter prototype. In *Journal of Physics: Conference Series*, volume 1162, page 012012. IOP Publishing, 2019.

[14] Antoine Laudrain and CALICE Collaboration. The calice ahcal: a highly granular sipm-on-tile hadron calorimeter prototype. In *Journal of Physics: Conference Series*, volume 2374, page 012017. IOP Publishing, 2022.

[15] A White, J Yu, G Eigen, J Zalieckas, D Dannheim, K Elsener, C Grefe, W Klempt, L Linssen, A Sailer, et al. Design, construction and commissioning of a technological prototype of a highly granular sipm-on-tile scintillator-steel hadronic calorimeter. *Journal of Instrumentation*, 18(11):P11018, 2023.

[16] Yukun Shi, Yunlong Zhang, Manqi Ruan, and Jianbei Liu. Design and optimization of the cepc scintillator hadronic calorimeter. *Journal of Instrumentation*, 17(11):P11034, 2022.

[17] L Li, Q Shan, W Jia, B Yu, Y Liu, Y Shi, et al. Optimization of the cepc-ahcal scintillator detector cells, 2021.

[18] Xi-Yang Wang, Hong-Yu Zhang, De-Qing Fang, Wan-Bing He, Xiao-Long Wang, Qi-Bin Zheng, and Shi-Ming Zou. Design and performance of a high-speed and low-noise preamplifier for sipm: Xy. wang et al. *Nuclear Science and Techniques*, 34(11):169, 2023.

[19] Anshun Zhou, Zhongtao Shen, Yukun Shi, and Shubin Liu. The single-layer readout electronics design and development for cepc scintillator analog hadronic calorimeter prototype. *Journal of Instrumentation*, 18(05):P05001, 2023.

[20] Xin Xia, Baohua Qi, Manqi Ruan, Yong Liu, and Yuzhi Che. Pattern recognition at cepc ahcal prototype using beam test data at cern. In *EPJ Web of Conferences*, volume 320, page 00047. EDP Sciences, 2025.